Analysis of the shear stresses in a filling line of parenteral products: the role of sterilizing filters

(Article begins on next page)

03 September 2024

Analysis of the shear stresses in a filling line of parenteral products: The role of sterilizing filters

Camilla Moino [a], Enrico Agostini [a], Andrea Albano [b], Marco Bellini [c], Erwan Bourlès [c], Bernadette Scutellà [c], Gianluca Boccardo [a], Roberto Pisano [a],*

[a] Department of Applied Science and Technology, Politecnico di Torino, 24 Corso Duca Degli Abruzzi, Torino 10129, Italy
[b] GSK, 1 Via Fiorentina, Siena 53100, Italy
[c] GSK, 89 Rue de L'Institut, Rixensart 1330, Belgium

ARTICLE INFO

ABSTRACT

This study investigates the impact of shear stress on protein-based parenteral drug products, particularly during the filling process, with a focus on the filtration unit. A 3D computational replica of a real sterilizing filter was developed using a stochastic geometry generation methodology, able to replicate realistic values of permeability, porosity, and pore size distribution. Computational Fluid Dynamics simulations were employed to analyze fluid dynamics within the filtration unit. The evolution of shear stress for massless tracers was examined to assess average shear stress in the sterilizing filtration unit. The results provide insights into shear stress dynamics and suggest potential scale-down strategies for industrial applications. The presented analysis is novel compared to most estimations of shear stress in sterilizing filtration units, which generally rely on mathematical calculations.

1. Introduction

Drug manufacturing consists of a series of operations, generally referred to as formulation, fill and finish. First, the purified form of the drug product is formulated with selected excipients, then it is filled into vials or syringes and is ready for packaging, labelling and quality inspection before distribution [1]. Among the other operations, the filling step represents the most critical one, in which the pharmaceutical drug product undergoes different stages, including mixing, pumping, filtration, and final filling into vials. As filling lines continue to operate under more and more accelerated conditions, there is great concern over stability of protein-based products [2,3]. They may be sensitive to temperature changes, oxidation, light, ionic strength and shear stress [4]. Computational Fluid Dynamics (CFD) investigation of some of the typical unit operations (product flowing in tubing and sampling through fittings) has been already published from our research group [5,6]. However, one of the most challenging steps to analyse is the filtration process. Filtration plays a critical role in guaranteeing the absence of microbiological or particle contamination in the product. This pressure-driven process pushes the product across a semi-permeable membrane in an effort to separate the contaminants from the solution [7] and has been broadly studied in the literature for various applications [8–10].

In the realm of bioprocessing steps, more specifically, there are various types of filtration; among them dead-end filtration has wide use in bioprocessing [11]. In particular, sterile filtration is widely used for parenteral drug products to verify they meet the sterility criterion. It specifically allows the complete retention of a microbiological challenge with 10^7 colony forming units/cm^2 of filter area [12]. In accordance with the Food and Drug Administration and the United States Pharmacopoeia guidelines, sterilizing filters should be product compatible [13] and made of non-fiber releasing materials with a nominal rating of 0.2 μm and 0.22 μm respectively [14,15]. Such membranes can be placed in different housings, depending on the need. Typically, studies for initial screening and preliminary filter sizing are performed using flat membrane discs [16]. At manufacturing scale, on the other hand, capsule [11],cartridge [17] filters with membrane pleating are generally employed; the pleating allows a larger area of the filter medium to be packed in such a way to increase performance in terms of fluid flowrate and total throughput, meaning the amount of fluid which can be processed before the filtration is stopped [18,19]. For the sake of clarity, an example of these membranes is given in Fig. 1. Such membranes have a characteristic thickness of hundreds of μm and a length on the order of *cm*.

Scale-up is necessary to pass from bench-scale to manufacturing-scale and vice versa for scale-down [17]. Linear scale-up (or scale-

Nomenclature

A	streamline area of influence, m^2
C	filtration capacity, m^3
CV	coefficient of variation, -
d_c	cell diameter, m
d_w	window diameter, m
D_{pore}	mean pore diameter, m
EFA	Effective Filtration Area, cm^2
g	gravity, m s^{-2}
k	porous medium permeability, m^2
m	number of streamlines, -
p	fluid pressure, Pa
$\Delta P/L$	pressure drop over porous medium length, kg m^{-2} s^{-2}
Q	volumetric flowrate, mL min^{-1}
Re	Reynolds number, -
St	Stokes number, -
SF	Safety Factor, -
t	time, s
u	fluid velocity, m/s
u_{pore}	pore-scale velocity, m/s
V	Darcy velocity, m/s
w	volumetric flowrate weight, m^3/s
x	spatial coordinate, m

Greek letters

α	coefficient of proportionality, -
γ	shear rate, s^{-1}
ε	porous medium porosity, -
μ	dynamic fluid viscosity, kg m^{-1} s^{-1}
ν	kinematic fluid viscosity, m^2/s
ρ	fluid density, kg m^{-3}
σ	shear stress, Pa
τ	residence time, s
τ_f	fluid time scale, s
τ_P	particles response time, s

Subscripts

comm	commercial
i	index
j	index
lab	laboratory
ms	microscale
ta	time-averaged
theo	theoretical
tot	total

Abbreviations

CFD	Computational Fluid Dynamics
CLSM	Confocal-Laser-Scanning Microscopy
CT	Computed Tomography
SEM	Scanning Electron Microscopy
TEM	Transmission Electron Microscopy

down) assumes that the filtration area increases proportionally to the volume of the solution to be processed; however, a more thorough understanding of scale-up from discs to pleated filters has become necessary and is generally referred to as Safety Factor (*SF*) [20]. It considers both the Effective Filtration Area (*EFA*) and the filtration capacity (*C*), i. e., the cumulative filtrate volume, as follows:

$$SF = \frac{\left(\frac{EFA}{C}\right)_{comm}}{\left(\frac{EFA}{C}\right)_{lab}} \qquad (1)$$

where *comm* and *lab* stand for commercial and laboratory scale, respectively.

This factor is introduced to minimize the risk of underestimating the filter area and compensate the variability usually connected with upscaling processes, which include differences in flow geometries, extra-membrane flow resistances, and fouling phenomena [21]. There is a wide range of potential *SF* and a thorough list is reported in Haindl et al. [22] who found values from 0.75 to 2.5 in their review of the literature, although calculations performed on different filters gave them a much higher *SF* (7.17).

Membrane characterization is fundamental to gain insights into the porous structure and get medium properties, such as porosity, mean pore size and pore size distribution. In addition, it can be used to inform computer simulations of digital structure reconstruction in an effort to obtain a realistic representation of the porous media. This characterization can be performed through several techniques, including Scanning Electron Microscopy (SEM), tomography, and Confocal-Laser-Scanning Microscopy (CLSM) [23]. In particular, SEM is a magnification tool which makes use of focused beams of electrons to obtain
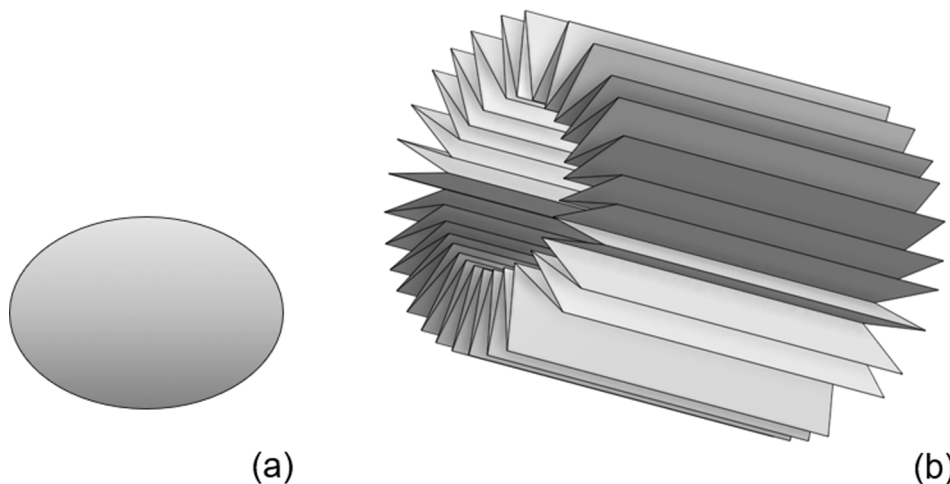

Fig. 1. Example of flat membrane (a) used in the disc configuration and pleated membrane (b) in capsule / cartridge.

information on the porous structure. One of the missing features of SEM is that it only provides morphological information thus making it invaluable in getting 3D information. Similarly, Transmission Electron Microscopy (TEM) can provide high-resolution views of objects but is limited to 2D images and cannot identify 3D morphology of samples [24]. Another valuable technique is the nano/micro-Computed Tomography (CT) which does not need any invasive procedure prior to imaging and allows 3D characterization of the membrane [25]. There are different types of CT scanners that allow for different sample size and resolution, thus providing multiscale opportunities with CT. The typical resolution of micro-CT and nano-CT scanners, for instance, is around 1–100 μm and as low as 0.5 μm, respectively [26]. Similarly, CLSM can be employed for this purpose. After the 2D images of the 3D membrane are obtained, they are used in combination with computer-based image analysis to derive a complete 3D representation of the membrane structure, [23] which can be further used to perform CFD analysis. In a former work, Affandy [27] reports a case of 2D reconstruction of sterile filters passing through TEM images. For 3D reconstruction, on the other hand, the analyses went up to dimensions of 8 μm. As sufficiently high-resolution 3D images of the micro-structure of real porous membranes are difficult to obtain by tomographic methods, detailed studies are more and more based on 3D digitalized models, obtained by various stochastic reconstruction techniques [28–30].

As previously stated, CFD is being utilized more and more in pharmaceutical applications enabling process monitoring and optimization without the requirement for products [31]. In such a realm, two approaches are generally used to deal with a porous medium, named 'microscale' and 'macroscale' approaches. The first strategy takes into account the actual pore size and morphology inside the membrane or the porous medium in general, which contributes to a complex fluid dynamics behavior of the fluid [32,33]. The macroscale approach, on the other hand, is an averaged representation of the pore-scale process and is a computationally efficient alternative to microscale model [34,35]; however, it is not suitable to detect local fields through the pores, i.e., shear stresses. For this reason, a microscale framework was chosen for the present analysis.

In this manuscript, a 3D reconstruction of a sterilizing membrane used in biopharmaceutical applications is obtained based on experimental data, i.e., pore size distribution, porosity, and permeability. Then, models for the shear stress distribution derived in a former work from our research group [6] are applied in order to assess the average shear stress that the fluid experiences when flowing through the medium in a microscale framework. This led to a relation between the Darcy velocity in the porous medium (V_{ms}) and the resulting shear stress, which is applicable to the membrane filter under investigation. Finally, considerations on the applicability of scale-down strategies for this unit operation are provided. To the best of our knowledge, this analysis is brand-new compared to most shear stress estimations in filtration units, which generally rely on mathematical calculations [36,37].

2. Governing equations and theoretical background

As suggested elsewhere [38], although the characteristic length of the pores of the membrane is rather small, i.e., in the order of hundreds of *nm*, the continuum hypothesis still holds true. The transport phenomena inside the pores are governed by the continuity equation and the Navier-Stokes equation. In the case of an incompressible fluid flowing through the void fraction of the geometry with constant density and viscosity, these equations read as follows:

$$\frac{\partial u_i}{\partial x_i} = 0 \tag{2}$$

$$\frac{\partial u_i}{\partial t} + u_j \frac{\partial u_i}{\partial x_j} = -\frac{1}{\rho}\frac{\partial p}{\partial x_i} + \nu \frac{\partial^2 u_i}{\partial x_j^2} \tag{3}$$

where u_i is the ith component of the fluid velocity, p is the fluid pressure and ρ and ν are its density and kinematic viscosity, respectively.

Simulation results are then interpreted based on macroscale continuum equations for fluid flows in porous media. The parameters of these spatially smoothed equations (e.g., porosity and permeability) are derived from averaging procedures performed on the microscopic governing equations of both the porous medium and fluid flow, as explained by Whitaker [35]. Thus, **Equations (2) and (3)** become:

$$\frac{\partial V_i}{\partial x_i} = 0 \tag{4}$$

$$\frac{\partial V_i}{\partial t} + V_j \left(\varepsilon \frac{\partial V_i}{\partial x_j}\right) = -\frac{1}{\rho}\frac{\partial p}{\partial x_i} + g_i + \frac{\nu}{k}V_i \tag{5}$$

where V_i is the Darcy velocity in the porous medium, ε the medium porosity, and k the membrane permeability. Assuming the flow is stationary, the regime is laminar – as demonstrated in the next paragraph – and the gravity effects are unimportant, some terms can be neglected; this leads to the well-known Darcy's Law written as a 1D expression:

$$\frac{\Delta P}{L} = -\frac{\mu |V|}{k} \tag{6}$$

where $\Delta P/L$ is the pressure drop over the length of the porous medium and μ is the dynamic fluid viscosity.

3. Experimental set up

Experimental work was conducted to assess the permeability of a typical sterilizing membrane used for filling purposes. The Durapore membrane [39] was adopted, being a membrane with homogeneous average pore size, without upstream / downstream side, like other membrane in Polyether Sulfone (PES) for instance [40]. It is a hydrophilic Polyvinylidene Fluoride (PVDF) membrane used for applications requiring the highest degree of sterility assurance.

Many different housing configurations are available for such membrane, including cartridges, capsules, and disc membrane [41]. This last membrane has a porosity (ε) of 70 %, a depth of 125 μm and a diameter of 47 mm. SEM was used to assess the surface and cross-sectional morphologies of the sterilizing membrane. For cross-section images, the samples were cut in liquid nitrogen using a sharp knife. This analysis provided an idea of the morphology of the structure and proved the uniformity of the pore size distribution. An example of cross-section image is shown in Fig. 2, while Fig. 3 shows the experimental set up used in this study for the estimation of the membrane permeability; a
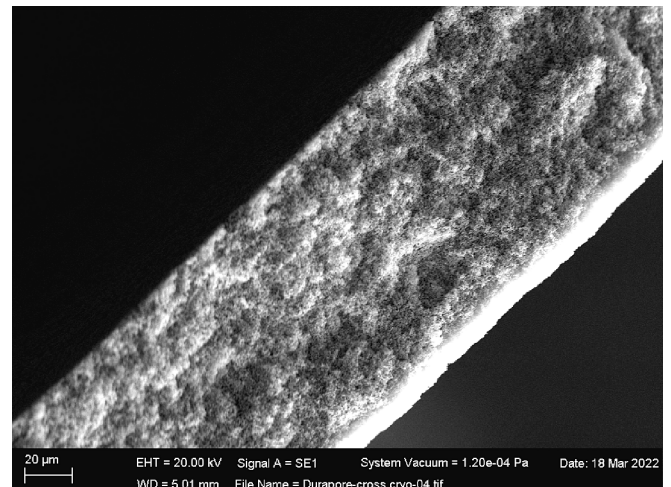

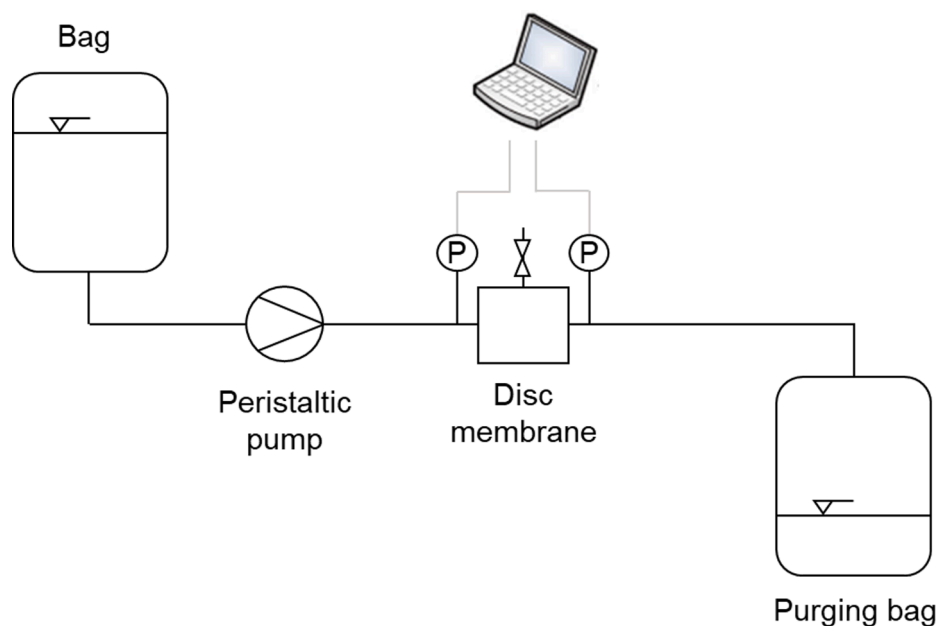**Fig. 2.** SEM cross-section of the Durapore membrane.

Fig. 3. Experimental set up that has been used for the estimation of the pressure drop across the membrane given a certain flowrate and, thus, its permeability.

Watson Marlow peristaltic pump was used to drive water across the disc (with Durapore membrane) at different flowrates.

Pressure sensors (P) were used to detect the pressure drop across a membrane filter when water was flowing through the circuit at different flowrates. The relationship between the inlet flowrate and the resulting pressure drop was found out to be linear, i.e., laminar condition [42], and the trend is displayed in Fig. 4. Three trials for each flowrate were run on clean membranes to account for experimental variance and the relevant coefficients of variation (*CV*) are also reported. For clarity, a

Fig. 4. Pressure drop vs flowrate for three different data sets through the Durapore membrane in (a). Each data set is represented by a geometric figure (circle, square, pentagon). Coefficients of variation *CV* are reported in (b).

higher *CV* can be observed for the 20 mL min^{-1} flowrate, which could be due to an experimental uncertainty in one of the three samples and the limited number of experimental data sets. Nonetheless, although higher than the other flowrates investigated, the *CV* at 20 mL min^{-1} is still small and the overall linear trend in the pressure drop is preserved. Therefore, the pressure drop with the lowest *CV* was then selected, i.e., that at 40 mL min^{-1}, and it was used to calculate the membrane *k* using the previously reported **Equation (6)**.

The estimated permeability was 2.63×10^{-15} m^2. It must be noted that *k* assessed with such experiments considers both the resistance provided by the filter housing and the membrane pores. Nonetheless, as suggested elsewhere [43], the filter housing resistance was assumed to be negligible because the pores undoubtedly make up the major contribution.

4. Numerical set up

In this work, a computational replica was achieved using the code developed previously by one of the authors and available in [44], which makes use of the software plugIm! (https://www.plugim.fr/). For the computational analysis of fluid flow, on the other hand, the finite volume method-based open-source code OpenFOAM 9 (https://github.com/OpenFOAM/OpenFOAM-9) was used. The simulations were carried out on an HP workstation with eight logical processors and 16 GB of RAM. Python 3.8 was used for the post-processing of the simulations. For the sake of clarity, the details for the membrane and grid generation are reported in two separate sections (Sections 4.1 and 4.2).

4.1. Membrane generation

The workflow used for the development of the computational replica [44] is composed of three distinct processes, including sphere aggregation, Voronoi tessellation, and concluding morphological operations. The number of spheres for the aggregation with the relative cell diameter (d_c), the repulsion factor (*Repul*), the size of the spheres and cylinders for the Voronoi tessellation (R_{node}, R_{strut}), and the resolution of the box were some of the parameters that were tuned.

Some details of the membrane are represented in Fig. 5, which zooms on the representative cell.

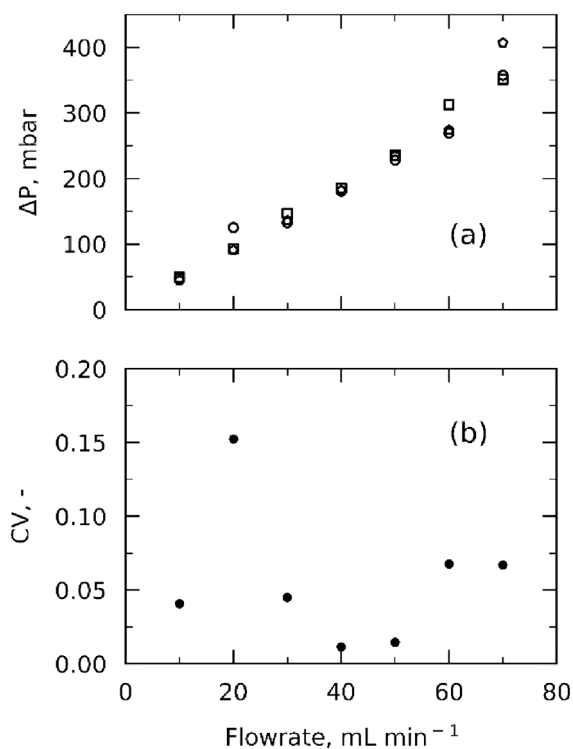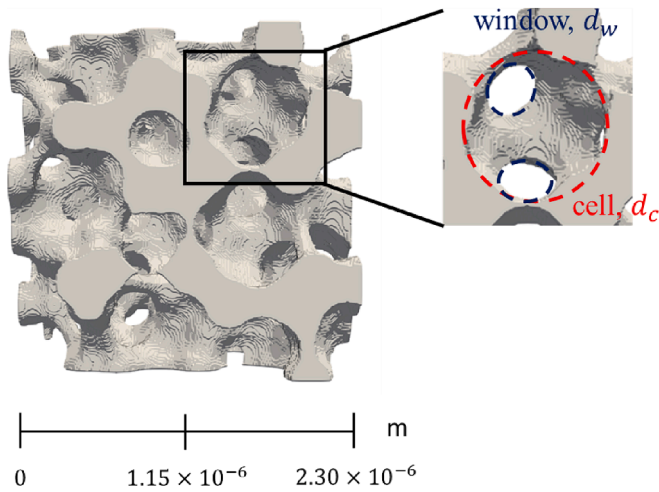As a starting point, it was assumed that the given pore size equals the

Fig. 5. Cell unit of the membrane showing its components.

window diameter (d_w), which delimits the area where the fluid passes through. The relation between cells diameter and window diameter was found in Inayat et al. [45]:

$$d_w = \frac{d_c}{2.3} \tag{7}$$

and it was therefore used to assess d_c for the initial sphere aggregation.

Based on [44], the dimension of the box was chosen equal to five times the d_c; this value was found high enough so as to ensure the chosen computational domain is a representative elementary volume, which is defined as a volume surrounding a point in which all averaged attributes are independent on the size of the volume [46].

The structure was developed to meet the actual ε (provided by manufacturer) and experimental k. An iterative workflow was used until the desired ε and k were both achieved (Fig. 6).

For the sake of clarity, Table 1 reports the dimensionless parameters that yielded the desired values for ε and k.

Further analysis on the membrane were carried out, using the poreSpy module available in python, which is a toolkit for microstructure investigation of porous media [47]. The resulting pore size distribution is shown in Fig. 7, and it is consistent with experimental data from the literature [48].
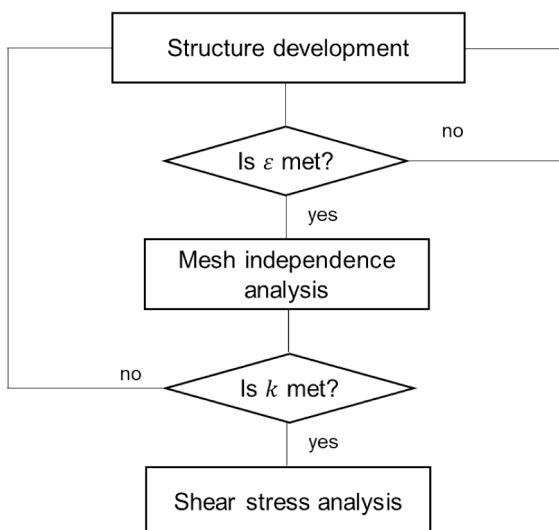

Fig. 6. Numerical set up.

Table 1
Dimensionless parameters used in structure development.

| Parameter	Meaning	Value
NB	Initial number of spheres	380
Alpha	Compactness parameter	0.55
Beta	Compactness parameter	0.75
Repul	Repulsion	20
R	Sphere diameter	25
W	Box size	250
R_{node}	Sphere diameter for the tessellation	17
R_{strut}	Cylinder diameter for the tessellation	6
Operation	Morphological operation	Closing
Iter	Number of iterations for the tessellation	1
$t\nu$	Size of the chosen morphological operation	19
vx_{res}	Voxel resolution	9.2×10^{-9}
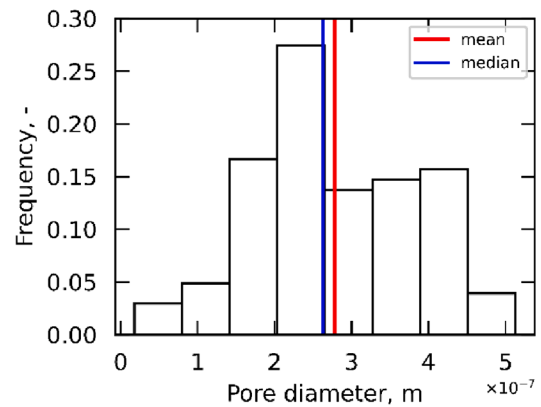
Fig. 7. Pore size distribution. The mean and median values (2.8×10^{-7} and 2.6×10^{-7} m, respectively are also shown).

4.2. Grid generation

Pre-mixing and post-development regions are added to ensure development of the flow prior to and past the actual membrane, as
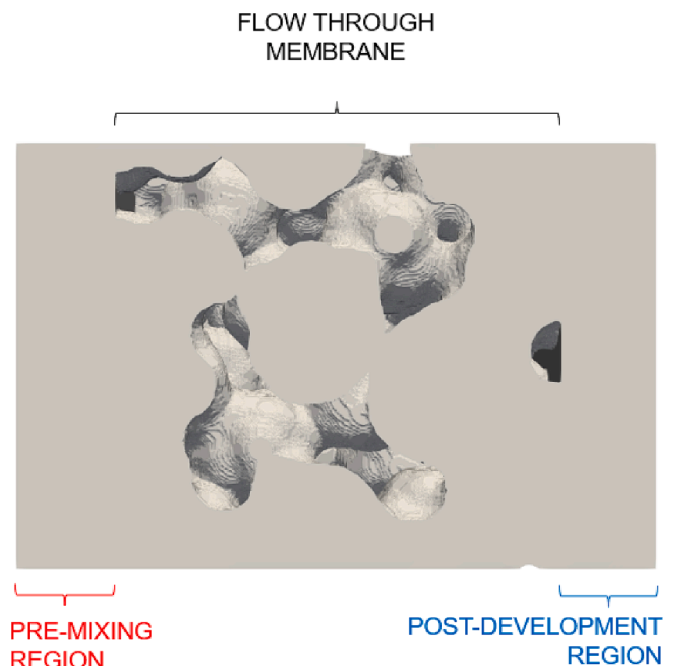

Fig. 8. Computational domain. Pre-mixing and post-development regions are shown.

shown in Fig. 8 where the computational domain is displayed.

Special emphasis should be given to the boundary conditions, summarized in Table 2.

A Newtonian incompressible fluid with water-like properties [49] was considered. Steady-state conditions were assumed and the solver *simpleFoam* was used to perform the fluid flow simulations. Based on the initial experimental investigation reported in Section 3, laminar regime was considered, where Reynolds number (*Re*) was evaluated as follows:

$$Re = \frac{\rho u_{pore} D_{pore}}{\mu} \tag{8}$$

where u_{pore} is the pore-scale velocity and D_{pore} is the mean pore diameter of the membrane, defined as the diameter of a sphere having the same volume as the mean pore. Darcy's velocity (or surface velocity) in the porous medium (V_{ms}) was chosen from standard commercial filtration values using the following scaling equation:

$$\left(\frac{Q}{EFA}\right)_{comm} = \left(\frac{Q}{EFA}\right)_{ms} \tag{9}$$

where *EFA* is the Effective Filtration Area of the filter. For the commercial scale, capsules with *EFA* 864 and 6000 cm^2 respectively were considered and several operating conditions were tested ($Q = 2500$ mL min^{-1}, 1700 mL min^{-1}).

The membrane grid was developed by using two OpenFOAM utilities, named *blockMesh* and *snappyHexMesh*. The former is used to build a background structured hexahedral mesh, which is then used as a starting point to build a body-fitted grid via *snappyHexMesh*. The final grids were mainly comprised of hexahedral cells in such a way to ensure a good numerical performance of the solver. The grids were further refined close to the solid walls of the pores, thus resulting in cells of decreasing dimension moving from the pores walls to the bulk of the fluid.

A grid independence analysis was conducted to find the optimal mesh, resulting from a trade-off between computational cost and solution's accuracy. This was done by tuning two main parameters: the number of background cells in the initial background mesh and the level of refinement *Ref* performed by *snappyHexMesh* on the cells close to the solid pore surface. The values of the refinement level taken into account were $Ref = \{0, 1, 2\}$. The grid independence study was conducted by monitoring the pressure drop across the membrane, and the results are presented in Fig. 9, where the relative errors to the most computationally expensive grid are also shown for comparison.

It can be noted that $Ref = \{0\}$ does not lead to an accurate solution. Therefore, a more computationally expensive mesh should be used. On the other hand, grids corresponding to $Ref = \{1, 2\}$ and a number of cells higher than 2×10^6 seem to result in more accurate and converging solution. For the subsequent analysis, the mesh with $Ref = \{2\}$ and around 1.9×10^6 cells was used. This led to a k of 2.55×10^{-15} m^2, with a small percent relative error with respect to the experimental value reported in Section 3, i.e., 3%.

Having as objective the evaluation of viscous stresses, an investigation of the microscale of the membrane became necessary. As mentioned, macroscale models solve equations for macroscopic, and thus averaged, quantities. Therefore, when a closer look at local quantities at the scale of the pores is needed, microscale investigations like the present one need to be performed.

5. Results

5.1. Streamlines and shear stress analysis

Drawing on earlier works [5,6], innovative strategies were used to track biological particles of fluid through their trajectories and detect their relevant fields. This made it possible to develop shear stress statistics which accounted for the actual shear stress history of each individual particle. Therefore, the Stokes number (*St*) for these particles was initially estimated; this correlates the particles response time (τ_P) and the fluid time scale (τ_f), as follows:

$$St = \frac{\tau_P}{\tau_f} \tag{10}$$

The biological particles in the drug products have a density similar to water [49], and their size is smaller than 200 nm [50]. This results in *St* below the unity for all the operating conditions described. In such conditions, biological particles are expected to follow fluid streamlines closely and, therefore, massless tracers were used for the investigation. More specifically, the utility 'Stream tracer with custom source' available in ParaView [51] was utilized, whose seed points were randomly given as an input in the pre-mixing region. To provide an example, Fig. 10 shows the streamlines for 200 seeds.

Local fields across each streamline were then acquired through post-processing python scripts. A typical pore-scale velocity path is displayed in Fig. 11 **(a)**; local velocity and shear trends for such streamline can be observed in Fig. 11 **(b)**.

It can be noted from Fig. 10 that local fields greatly vary through the geometry because of the complexity (and tortuosity) of the membrane structure; therefore, as cumulative definitions appeared too sensitive to domain size and hardly applicable [6], an average shear stress per streamline is calculated, as reported in **Equation (11)**. The trapezoidal rule was used to estimate the integral and implemented through the 'trapz' function available in the numpy module in python. The averaged shear stress σ_i per streamline was therefore evaluated by time-averaging the shear stress along the streamline and using the relative flowrate w_i as weight.

$$\overline{\sigma}_i = \sum_i \left(\left(\frac{1}{\tau_i} \int_0^{\tau_i} \sigma_i(t) dt \right) \bullet \frac{w_i}{w_{tot}} \right) \tag{11}$$

$$w_i = A_i \frac{1}{\tau_i} \int_0^{\tau_i} u_i(t) dt \tag{12}$$

with $u_i(t)$ being the velocity at the relevant time step, i the streamline index. For the sake of clarity, the time-averaged shear stress introduced in **Equation (11)** will be referred to as $\sigma_{ta,i}$.

The average shear stress $\overline{\sigma}$ is then simply assessed as follows:

$$\overline{\sigma} = \frac{1}{m} \sum_i \overline{\sigma}_i \tag{13}$$

where m is the number of streamlines.

This weighing operation helped to consider streamline contributions to shear stress in a manner proportional to the actual flowrate through that specific point in the membrane.

An analysis was first conducted to find the minimum number of particles to release in order to fully describe the whole fluid dynamics within the membrane. A varying number of seeds was then released in the pre-mixing region and $\overline{\sigma}$ was monitored, as displayed in Fig. 12. Twenty trials with varying seed location were run for each number of seeds, and the related *CV* is reported.

The higher the number of seeds was, the lower the uncertainty span in $\overline{\sigma}$ was. From 200 seeds onwards, *CV* was bounded between 0 and 0.025 and, therefore, the number of seeds can be claimed sufficient to

Table 2
Boundary conditions for the main patches, expressed in terms of OpenFOAM classes.

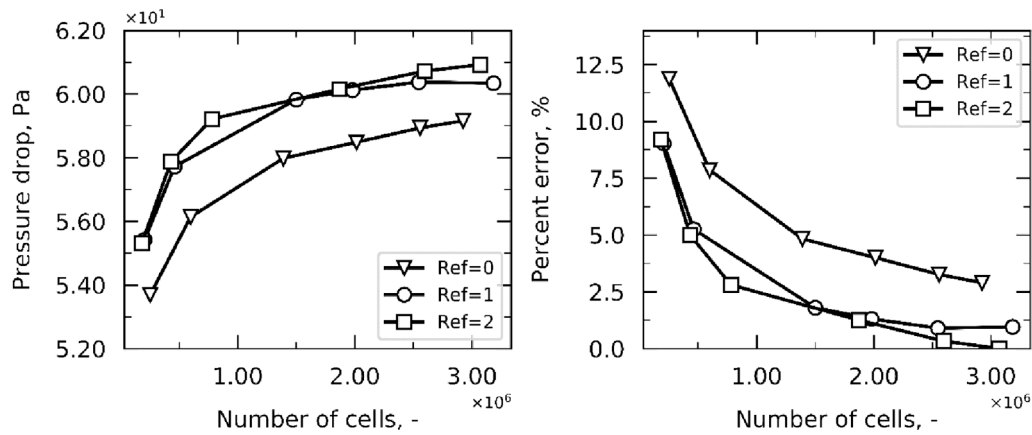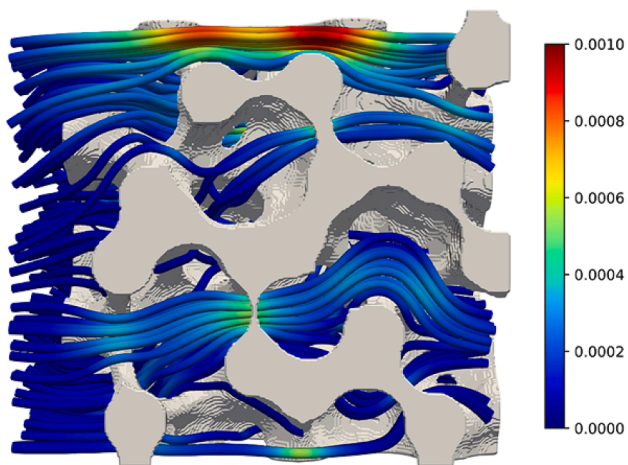| Patch	Boundary Condition	
	p	*u*
inlet	zeroGradient	fixedValue ($\overline{u}$)
outlet	fixedValue (0)	zeroGradient
wall	zeroGradient	noSlip
sides	symmetry	symmetry

Fig. 9. Grid independence analysis.

Fig. 10. 200 streamlines are followed through the porous medium and the local velocities are displayed.

describe the fluid dynamics within the membrane. 460 streamlines were finally chosen as the increase in the seeds number did not lead to a significant increase in the computational expense. This can be observed in Fig. 12, where the time to compute each point is displayed; as expected, the computation time varies linearly with increasing number of streamlines but is still way lower than the overall simulation time (which is in the order of hours instead).

Fig. 13 shows the distribution of the time-averaged shear stress in the

case of 460 seeds. It can be noticed that the higher shear stresses were experienced only by a small portion of the solution because the majority was subjected to lower shear stresses.

5.2. Industrial considerations

The previously reported analysis was then repeated for other velocities and other filtration unit *EFA*, representative of potential manufacturing units, in order to investigate the relation between the inlet velocity and the resulting shear. To allow for comparison with literature data, the shear rate γ is estimated, which is simply σ/μ being incompressible fluid. The relevant results are reported in Table 3 where the relevant $\bar{\gamma}$ for each Q_{comm} is reported for comparison. In addition, Re is also estimated using **Equation (8)**, where u_{pore} is estimated based on the membrane porosity as follows:

$$u_{pore} = \frac{V}{\varepsilon} \tag{14}$$

Therefore, being the flow through the pores laminar, a linear relationship is found between the inlet velocity and the resulting shear rate and is represented by α. For the three runs, the percent difference in α is below 5%.

A comparison with literature data was finally drawn. Some mention shear rate around 10,000 s^{-1} [52,53], which is in line with our estimates for the last operating conditions considered in Table 3. These values are generally calculated assuming that the pore is a cylindrical tube with mean diameter D_{pore}:
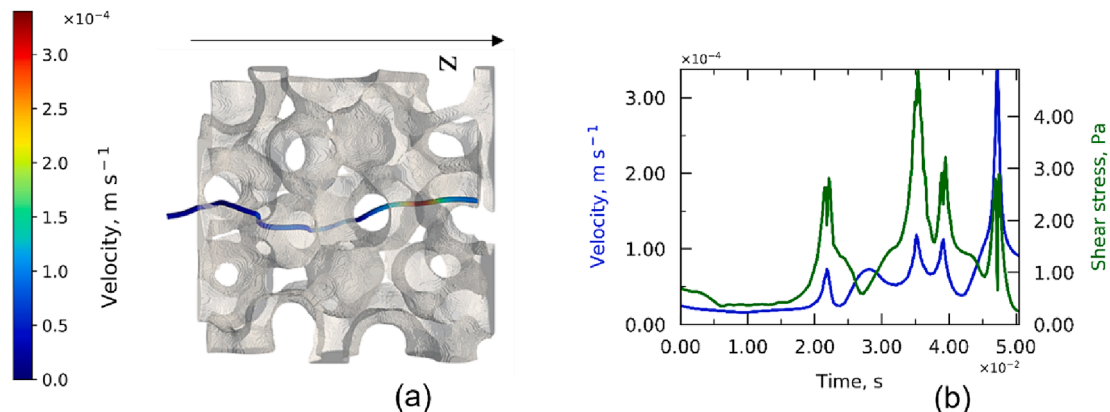

Fig. 11. Streamline for a hypothetical particle released in the pre-mixing region (a), with Z being the flow direction. Velocity (in blue) and shear stress (green) are displayed (b). (For interpretation of the references to color in this figure legend, the reader is referred to the web version of this article.)
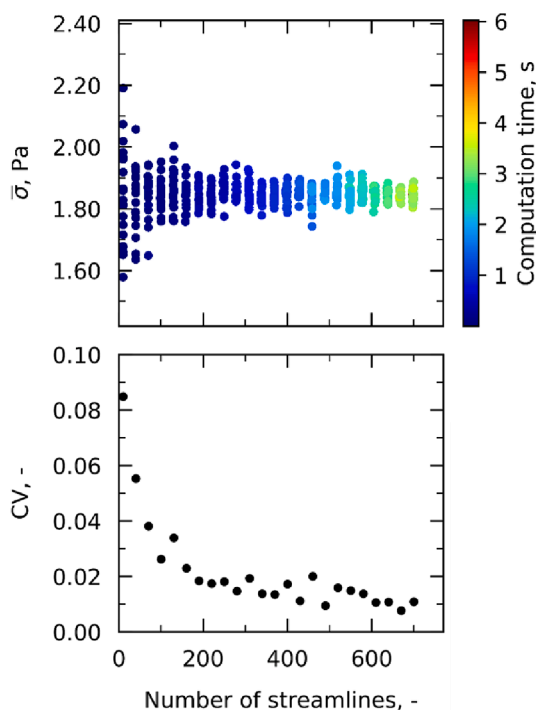
Fig. 12. Average shear stress $\overline{\sigma}$ is displayed while varying the number of streamlines and the number of trials to ease the visualization of the analysis in the top plot. Each point in the data set is colored based on its computation time (see color scale). Coefficients of variation *CV* are reported in the bottom plot.
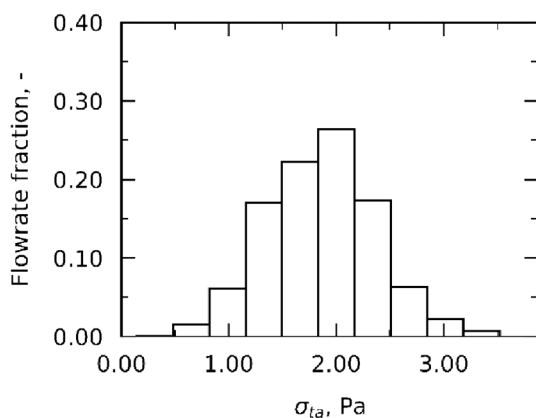

Fig. 13. The time-averaged shear stress (σ_{ta}) distribution for the analyzed filtration unit is displayed using the flowrate fraction (w_i) normalized over w_{tot} as weight.

Table 3
Results of the analysis for different commercial flowrates.

Q_{comm} mL min^{-1}	EFA_{comm} cm^2	V_{ms} m/s	Re	$\overline{\gamma}$ s^{-1}	$\overline{\gamma}_{theo}$ s^{-1}	α
2500	6000	6.94×10^{-5}	2.78×10^{-5}	1.85×10^3	2.40×10^3	26.7×10^6
1700	864	3.15×10^{-4}	1.26×10^{-4}	8.37×10^3	1.09×10^4	26.6×10^6
2500	864	4.63×10^{-4}	1.85×10^{-4}	1.29×10^4	1.60×10^4	27.7×10^6

$$\overline{\gamma} = \frac{16 u_{pore}}{3 D_{pore}} \tag{15}$$

Additionally, the workflow proposed in this manuscript allows for post-processing analysis to derive temporal and distribution information, which traditional equations (such as **Equation (15)** do not provide.

As expected [52], shear rates (and stresses) resulting from sterilizing filtration units are higher than those resulting from other filling line operations, such as flow through tubing and fittings, whose investigation was the focus of other works from our research group [5,6]. To provide some examples from these studies, shear rates of around 8×10^2 s^{-1} were found for flow in smooth tubing under turbulent conditions (flowrates around 2140 mL min^{-1} in 9.53-mm-tubing); similar values of shear rates were found for Y-fittings under the same operating conditions while higher for T-fittings (i.e., 1.2×10^3 s^{-1}). Under laminar conditions (flowrates around 180 mL min^{-1}), on the other hand, much lower shear rates were monitored (2×10^1 s^{-1}).

A final remark can be given regarding scaling approaches, which, as mentioned in the Introduction, are critical to ensure representativeness between laboratory and commercial scales without over- or under-estimating the system. As previously stated, they use appropriate scaling factors that account for differences in flow resistance, fouling phenomena, and flow geometries. Without exploring such macroscopic differences, however, the present work offers a formula for ensuring, at the microscopic level, that the product is exposed to the same shear stress in the laboratory compared to the commercial scale. For this particular filtration unit, being the flow laminar through the pores, the application of **Equation (16)** can guarantee that the local shear stresses at the microscale level are preserved if the same membrane type is used in the laboratory scale unit. Indeed, the ratio between the two quantities might differ from unity if other factors besides shear stresses are considered.

$$\left(\frac{Q}{EFA}\right)_{comm} = \left(\frac{Q}{EFA}\right)_{lab} \tag{16}$$

6. Conclusion

In the present work, CFD simulations were employed to investigate the fluid dynamics within a typical sterile filtration unit. A computational replica was obtained through stochastic membrane reconstruction to meet porosity, pore size distribution, and permeability of the real filter. Shear stress analyses were conducted and the average shear exposures of the product at different operating conditions were estimated. These values were compared with those derived from traditional simplified equations; not only are the values consistent, but the present workflow allows post-processing analyses (on residence time, shear stress distributions) that traditional equations do not provide. Also, as expected, when comparing these shear stresses with those from other components of the filling line, i.e., tubing, fittings, they appeared much higher. Considerations were also drawn on the scale-down operation for the pharmaceutical industry.

The methodology we proposed can be used to explore other areas. For instance, one could evaluate particle impingement in pores during long-term processes, where aggregation phenomena are prominent, or focus on regions of high shear stress. The work could further be extended to membranes with non-uniform pore distributions or pleated membrane deformation could be studied to make the analysis even more meaningful.

This research lays the foundation for future development prospects. The impact of monitored shear stress on product stability and separation efficiency could be investigated.

CRediT authorship contribution statement

Camilla Moino: Writing – review & editing, Writing – original draft, Visualization, Validation, Software, Methodology, Formal analysis, Conceptualization. **Enrico Agostini:** Writing – review & editing, Visualization, Validation, Software. **Andrea Albano:** Writing – review & editing, Methodology. **Marco Bellini:** Writing – review & editing, Methodology, Conceptualization. **Erwan Bourlès:** Writing – review & editing, Methodology, Conceptualization. **Bernadette Scutellà:** Writing – review & editing, Methodology, Conceptualization. **Gianluca Boccardo:** Writing – review & editing, Software, Methodology, Conceptualization. **Roberto Pisano:** Writing – review & editing, Methodology, Conceptualization.

Declaration of competing interest

The authors declare that they have no known competing financial interests or personal relationships that could have appeared to influence the work reported in this paper.

Data availability

Data will be made available on request.

References

[1] S.Y. Patro, E. Freund, B.S. Chang, Protein formulation and fill-finish operations, Biotechnol. Annu. Rev. 8 (2002) 55–84, https://doi.org/10.1016/S1387-2656(02)08004-3.
[2] F. Jameel, S. Hershenshon. Formulation and process development strategies for manufacturing biopharmaceuticals, John Wiley & Sons, Inc, Hoboken, New Jersey, NJ, USA, 2010, https://doi.org/10.1002/9780470595886.
[3] C. Moino, F. Artusio, R. Pisano, Shear stress as a driver of degradation for protein-based therapeutics: more accomplice than culprit, Int. J. Pharm. 650 (2024) 123679, https://doi.org/10.1016/j.ijpharm.2023.123679.
[4] WHO, Guidelines for stability testing of pharmaceutical products containing well established drug substances in conventional dosage forms, World Health Organ. Tech. Rep. Ser. (1996) 65–80.
[5] C. Moino, B. Scutellà, M. Bellini, E. Bourlès, G. Boccardo, R. Pisano, Analysis of the Shear stresses in a filling line of Parenteral products: the role of tubing, Processes. 11 (2023), https://doi.org/10.3390/pr11030833.
[6] C. Moino, B. Scutellà, M. Bellini, E. Bourlès, G. Boccardo, R. Pisano, Analysis of the Shear stresses in a filling line of Parenteral products: the role of fittings, Processes. 11 (2023) 1797, https://doi.org/10.3390/pr11061797.
[7] M.W. Jornitz, Filtration and purification in the pharmaceutical industry, third, CRC Press Taylor & Francis Group, Boca Raton, Florida, 2020.
[8] W. Chen, J. Mo, X. Du, Z. Zhang, W. Zhang, Biomimetic dynamic membrane for aquatic dye removal, Water Res. 151 (2019) 243–251, https://doi.org/10.1016/j.watres.2018.11.078.
[9] W. Zhang, W. Liang, Z. Zhang, T. Hao, Aerobic granular sludge (AGS) scouring to mitigate membrane fouling: performance, hydrodynamic mechanism and contribution quantification model, Water Res. 188 (2021) 116518, https://doi.org/10.1016/j.watres.2020.116518.
[10] W. Zhang, W. Liang, Z. Zhang, Dynamic scouring of multifunctional granular material enhances filtration performance in membrane bioreactor: mechanism and modeling, J. Memb. Sci. 663 (2022), https://doi.org/10.1016/j.memsci.2022.120979.
[11] M. Dixit, Membranes and filtration: membrane filtration in the biopharm industry, Filtr. Sep. 45 (2008) 18–21, https://doi.org/10.1016/S0015-1882(08)70294-5.
[12] M. Jornitz, T.H. Meltzer, Promoting patient safety, Pharm. Technol. Eur. 20 (2008) 41–45.
[13] S.Y. Kong, Plasmid DNA and bacterial artificial chromosomes processing for gene therapy and vaccination : studies on membrane sterile filtration, University College London, 2006.
[14] T.H. Meltzer, M.W. Jornitz, The sterilizing filter and its pore size rating, Am. Pharm. Rev. 1–5 (2003).
[15] M. Ramstorp. Contamination control in Practice, WILEY-VCH GmbH & Co. KGaA, Weinheim, Germany, 2003, https://doi.org/10.1002/9783527612604.
[16] S. Giglia, D. Yavorsky, Scaling from discs to pleated devices, PDA J. Pharm. Sci. Technol. 61 (2007) 314–323.
[17] A. Kumar, J. Martin, R. Kuriyel, Scale-up of sterilizing-grade membrane filters from discs to pleated cartridges: effects of operating parameters and solution properties, PDA J. Pharm. Sci. Technol. 69 (2015) 74–87, https://doi.org/10.5731/pdajpst.2015.01006.
[18] J. Dippel, S. Handt, B. Stute, E. von Lieres, T. Loewe, Fluid dynamics in pleated membrane filter devices, Sep. Purif. Technol. 267 (2021) 118580, https://doi.org/10.1016/j.seppur.2021.118580.
[19] A.I. Brown, P. Levison, N.J. Titchener-Hooker, G.J. Lye, Membrane pleating effects in 0.2 μm rated microfiltration cartridges, J. Memb. Sci. 341 (2009) 76–83, https://doi.org/10.1016/j.memsci.2009.05.044.
[20] Z. Du, S.P. Motevalian, B. Carrillo Conde, K. Reilly, A.L. Zydney, Scale-up issues during sterile filtration of glycoconjugate vaccines, Biotechnol. Prog. 38 (2022) 1–7, https://doi.org/10.1002/btpr.3260.
[21] S. Giglia, K. Rautio, G. Kazan, K. Backes, M. Blanchard, J. Caulmare, Improving the accuracy of scaling from discs to cartridges for dead end microfiltration of biological fluids, J. Memb. Sci. 365 (2010) 347–355, https://doi.org/10.1016/j.memsci.2010.09.032.
[22] S. Haindl, J. Stark, J. Dippel, S. Handt, A. Reiche, Scale-up of microfiltration processes, Chem.-Ing.-Tech. 92 (2020) 746–758, https://doi.org/10.1002/cite.201900025.
[23] A. Ley, P. Altschuh, V. Thom, M. Selzer, B. Nestler, P. Vana, Characterization of a macro porous polymer membrane at micron-scale by confocal-laser-scanning microscopy and 3D image analysis, J. Memb. Sci. 564 (2018) 543–551, https://doi.org/10.1016/j.memsci.2018.07.062.
[24] P.M.V. Raja, A.R. Barron, Physical methods in chemistry and nano science, LibreTexts. (2023). https://chem.libretexts.org/Bookshelves/Analytical_Chemistry/Physical_Methods_in_Chemistry_and_Nano_Science_(Barron).
[25] L. Vásárhelyi, Z. Kónya, R.V. Kukovecz, Microcomputed tomography–based characterization of advanced materials: a review, Mater. Today Adv. 8 (2020) 1–13, https://doi.org/10.1016/j.mtadv.2020.100084.
[26] A. du Plessis, C. Broeckhoven, A. Guelpa, S.G. le Roux, Laboratory x-ray micro-computed tomography: a user guideline for biological samples, GigaScience 6 (2017) 1–11, https://doi.org/10.1093/gigascience/gix027.
[27] A. Affandy, Fundamental studies of the sterile filtration of large plasmid DNA, University College London, 2013.
[28] M.S. Talukdar, O. Torsaeter, M.A. Ioannidis, Stochastic reconstruction of Particulate media from two-dimensional stochastic reconstruction of Particulate media from two-dimensional images, J. Colloid Interface Sci. 248 (2002) 419–428, https://doi.org/10.1006/jcis.2001.8064.
[29] L.C. Capozzi, A. Arsiccio, A.C. Sparvigna, R. Pisano, A.A. Barresi, Image Segmentation and 3D reconstruction for improved prediction of the sublimation rate during freeze drying, in: IDS'2018–21st International Drying Symposium, 2018.
[30] E. Agostini, G. Boccardo, D. Marchisio, An open-source workflow for open-cell foams modelling: geometry generation and CFD simulations for momentum and mass transport, Chem. Eng. Sci. 255 (2022) 117583, https://doi.org/10.1016/j.ces.2022.117583.
[31] H.S. Pordal, C.J. Matice, T.J. Fry, The role of computational fluid dynamics in the pharmaceutical industry, Pharm. Technol. 26 (2002) 72–79.
[32] G. Boccardo, D.L. Marchisio, R. Sethi, Microscale simulation of particle deposition in porous media, J. Colloid Interface Sci. 417 (2014) 227–237, https://doi.org/10.1016/j.jcis.2013.11.007.
[33] A. Marcato, J.E. Santos, G. Boccardo, H. Viswanathan, D. Marchisio, M. Prodanović, Prediction of local concentration fields in porous media with chemical reaction using a multi scale convolutional neural network, Chem. Eng. J. 455 (2023) 140367, https://doi.org/10.1016/j.cej.2022.140367.
[34] I. Battiato, P.T. Ferrero V, D. O'Malley, C.T. Miller, P.S. Takhar, F.J. Valdés-Parada, B.D. Wood, Theory and applications of macroscale models in porous media, Transp. Porous Media. 130 (2019) 5–76, https://doi.org/10.1007/s11242-019-01282-2.
[35] S. Whitaker The Method of volume averaging 2013 Springer Science+Business Media.
[36] Y.-F. Maa, C.C. Hsu, Investigation on fouling mechanisms for recombinant human growth hormone sterile filtration, J. Pharm. Sci. 87 (1998) 808–812, https://doi.org/10.1021/js980114x.
[37] S. Nema, J.D. Ludwig, Pharmaceutical Dosage Forms, Third, Informa Healthcare, New York, NY, USA, 2010. https://doi.org/10.1002/14356007.a19_241.
[38] C. Liu, Z. Li, On the validity of the navier-stokes equations for nanoscale liquid flows: the role of channel size, AIP Adv. 1 (2011), https://doi.org/10.1063/1.3621858.
[39] Millipore Durapore Membrane Filter, 0.22 μm, (n.d.). https://www.merckmillipore.com/IN/en/product/Durapore-Membrane-Filter-0.22m,MM_NF-GVWP04700?bd=1 (accessed January 19, 2023).
[40] F. Fallahianbijan, P. Emami, J.M. Hillsley, S.P. Motevalian, B.C. Conde, K. Reilly, A.L. Zydney, Effect of membrane pore structure on fouling behavior of glycoconjugate vaccines, J. Memb. Sci. 619 (2021) 118797, https://doi.org/10.1016/j.memsci.2020.118797.
[41] Millipore, Durapore Family Guide, (n.d.). https://www.sigmaaldrich.com/deepweb/assets/sigmaaldrich/product/documents/764/350/durapore-family-guide-pg5075en-mk.pdf (accessed January 20, 2023).
[42] X. Xiao, A. Long, K. Qian, X. Zeng, T. Hua, Through-thickness permeability of woven fabric under increasing air pressure: theoretical framework and simulation, Text. Res. J. 87 (2017) 1631–1642, https://doi.org/10.1177/0040517516657062.
[43] E. Velali, J. Dippel, B. Stute, S. Handt, T. Loewe, E. von Lieres, Model-based performance analysis of pleated filters with non-woven layers, Sep. Purif. Technol. 250 (2020) 117006, https://doi.org/10.1016/j.seppur.2020.117006.

[44] E. Agostini, Fluid dynamics and mass transfer in porous media, Politecnico Di Torino (2023). https://iris.polito.it/handle/11583/2981457.

[45] A. Inayat, M. Klumpp, M. Lammermann, H. Freund, W. Schwieger, Development of a new pressure drop correlation for open-cell foams based completely on theoretical grounds: taking into account strut shape and geometric tortuosity, Chem. Eng. J. 704–719 (2012).

[46] Y. Bachmat, J. Bear, Macroscopic modelling of transport phenomena in porous media. 1: the continuum approach, Transp. Porous Media. 1 (1986) 213–240, https://doi.org/10.1007/BF00238181.

[47] J.T. Gostick, Z.A. Khan, T.G. Tranter, M.D. Kok, M. Agnaou, M. Sadeghi, R. Jervis, PoreSpy: A python toolkit for quantitative analysis of porous media images, J. Open Source Softw. 4 (2019) 1296, https://doi.org/10.21105/joss.01296.

[48] J. Na, D. Suh, Y.H. Cho, Y. Baek, Comparative evaluation of the performance of sterile filters for bioburden protection and final fill in Biopharmaceutical processes, Membranes 12 (2022) 524, https://doi.org/10.3390/membranes12050524.

[49] H. Fischer, I. Polikarpov, A.F. Craievich, Average protein density is a molecular-weight-dependent function, Protein Sci. 13 (2009) 2825–2828, https://doi.org/10.1110/ps.04688204.

[50] M.F. Bachmann, G.T. Jennings, Vaccine delivery: a matter of size, geometry, kinetics and molecular patterns, Nat. Rev. Immunol. 10 (2010) 787–796, https://doi.org/10.1038/nri2868.

[51] U. Ayachit. The ParaView Guide: A Parallel Visualization Application, Kitware Inc, 2018, p. 274.

[52] J.S. Bee, J.L. Stevenson, B. Mehta, J. Svitel, J. Pollastrini, R. Platz, E. Freund, J. F. Carpenter, T.W. Randolph, Response of a concentrated monoclonal antibody formulation to high shear, Biotechnol. Bioeng. 103 (2009) 936–943, https://doi.org/10.1002/bit.22336.

[53] W.T. Lowry, J.C. Garriott, Pharmaceutical dosage forms, in: Forensic Toxicology, Springer, Boston, MA, 1979, https://doi.org/10.1007/978-1-4684-3444-6_2.